

On-Surface Synthesis of Edge-Extended Zigzag Graphene Nanoribbons

Amogh Kinikar, Xiushang Xu, Marco Di Giovannantonio, Oliver Gröning, Kristijan Eimre, Carlo A. Pignedoli, Klaus Müllen, Akimitsu Narita,* Pascal Ruffieux, and Roman Fasel*

Graphene nanoribbons (GNRs) have gained significant attention in nanoelectronics due to their potential for precise tuning of electronic properties through variations in edge structure and ribbon width. However, the synthesis of GNRs with highly sought-after zigzag edges (ZGNRs), critical for spintronics and quantum information technologies, remains challenging. In this study, a design motif for synthesizing a novel class of GNRs termed edge-extended ZGNRs is presented. This motif enables the controlled incorporation of edge extensions along the zigzag edges at regular intervals. The synthesis of a specific GNR instance—a 3-zigzag-rows-wide ZGNR—with bisanthene units fused to the zigzag edges on alternating sides of the ribbon axis is successfully demonstrated. The resulting edge-extended 3-ZGNR is comprehensively characterized for its chemical structure and electronic properties using scanning probe techniques, complemented by density functional theory calculations. The design motif showcased here opens up new possibilities for synthesizing a diverse range of edge-extended ZGNRs, expanding the structural landscape of GNRs and facilitating the exploration of their structure-dependent electronic properties.

the electronic properties on the chemical structure of the GNRs, however, demands an atomically precise synthesis. This can be attained using surface-catalyzed chemical reactions that lead to the formation of covalent bonds between and within surface-adsorbed molecular building blocks. This so-called on-surface synthesis approach^[2,3] achieves atomic precision if only specific reactions are allowed, thus necessitating a careful design of molecular precursors used as building blocks. Therefore, the structural diversity of the GNRs that can be synthesized—and thus the structure-dependent properties that they can exhibit—relies critically on the available design motifs.^[1,4]


Homocoupling by forming a single C–C bond between molecular precursors is the simplest means toward the synthesis of extended one-dimensional structures. However, this necessarily leads to coupling along the armchair direction. Consequently, most of the GNRs that have been

synthesized to date are armchair GNRs (AGNRs). They have been fabricated with atomically pre-defined widths,^[5–9] chevron-like edges,^[5,10–13] and even with controlled heterostructure sequences.^[10,14–16] A few GNRs have also been grown along so-called chiral directions, i.e., along axes that deviate from the

1. Introduction

Graphene nanoribbons (GNRs) are an emerging class of nanomaterials with electronic properties that can be widely tuned by their width and edge structure.^[1] The sensitive dependence of

A. Kinikar, M. D. Giovannantonio^[+], O. Gröning, K. Eimre^[++],
C. A. Pignedoli, P. Ruffieux, R. Fasel
Empa
Swiss Federal Laboratories for Materials Science and Technology
nanotech@surfaces Laboratory
Dübendorf 8600, Switzerland
E-mail: Roman.Fasel@empa.ch

 The ORCID identification number(s) for the author(s) of this article can be found under <https://doi.org/10.1002/adma.202306311>

^[+]Present address: Institute of Structure of Matter – CNR (ISM-CNR), via Fosso del Cavaliere 100, 00133 Roma, Italy

^[++]Present address: EPFL, École polytechnique fédérale de Lausanne, NCCR MARVEL, Lausanne 1015, Switzerland

© 2023 The Authors. Advanced Materials published by Wiley-VCH GmbH. This is an open access article under the terms of the Creative Commons Attribution License, which permits use, distribution and reproduction in any medium, provided the original work is properly cited.

DOI: 10.1002/adma.202306311

X. Xu, A. Narita
Okinawa Institute of Science and Technology Graduate University
Organic and Carbon Nanomaterials Unit
1919-1 Tancha, Onnason, Kunigamigun, Okinawa 904-0495, Japan
E-mail: akimitsu.narita@oist.jp

X. Xu, K. Müllen, A. Narita
Max Planck Institute for Polymer Research
55128 Mainz, Germany

K. Müllen
Johannes Gutenberg University Mainz
Institute of Physical Chemistry
Duesbergweg 10-14, 55128 Mainz, Germany

R. Fasel
Department of Chemistry, Biochemistry and Pharmaceutical Sciences
University of Bern
Freiestrasse 3, Bern 3012, Switzerland

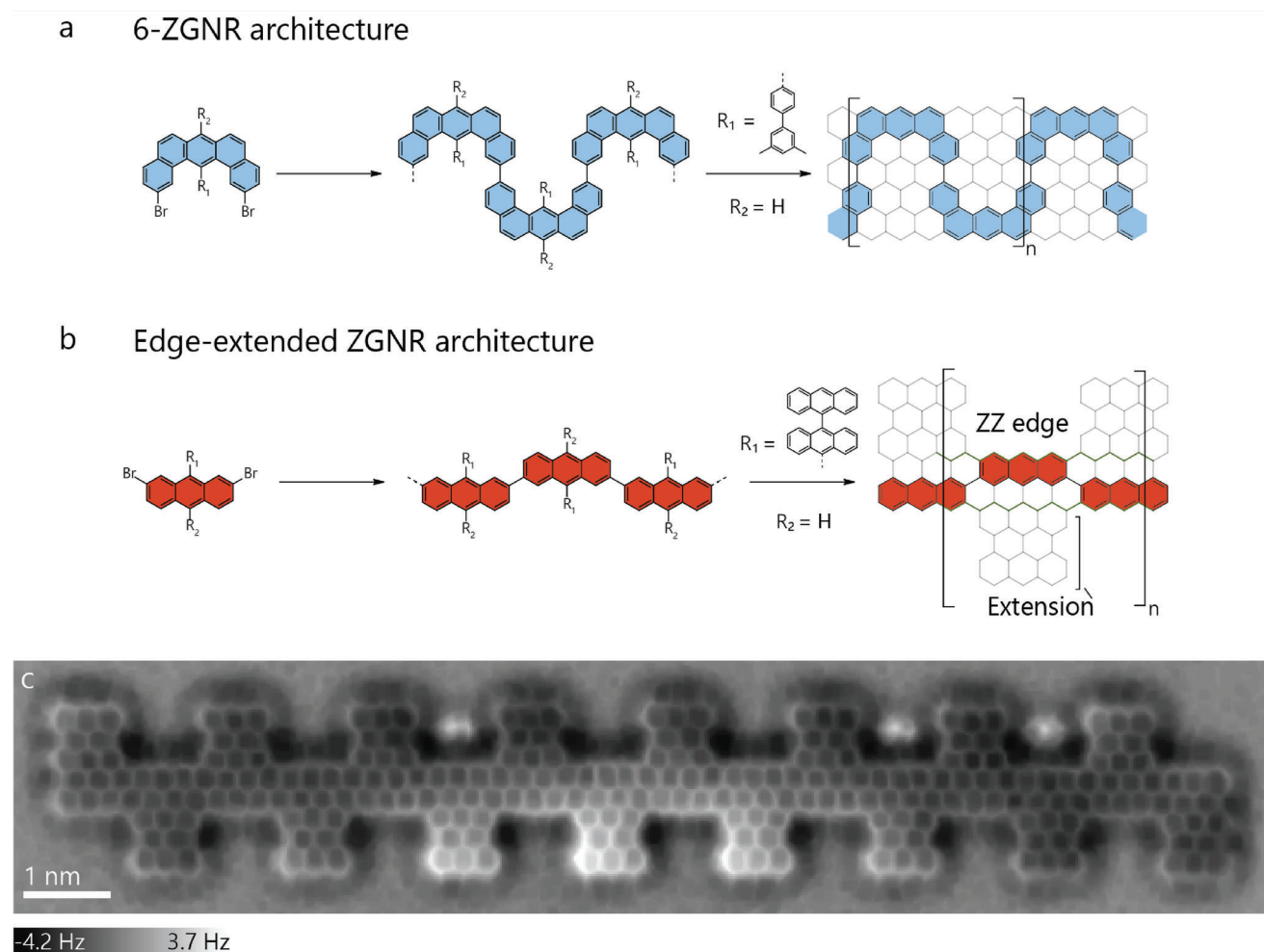


Figure 1. Design motifs to obtain ZGNRs and edge-extended ZGNRs. a) Atomically precise 6-ZGNRs have been synthesized using the polymer backbone of 2,12-linked-14- R_1 -7- R_2 -benzo[*m*]tetraphene polymer backbone. b) A new polymer backbone based on 2,7-linked-9- R_1 -10- R_2 -anthracene is demonstrated to synthesize edge extended ZGNRs. c) nc-AFM image of a 16-unit long 3-ZGNR-E(BA,7) confirms its chemical structure (nc-AFM image acquired in constant-height mode. Feedback switched off ($\Delta z = 0$) on top of the GNR with $V = 10$ mV and $I = 100$ pA). Color bar represents the frequency shift.

prototype armchair and zigzag directions.^[17–19] However, while such armchair and chiral GNRs have potential use in nanoelectronics because of their structure-tunable bandgap, zigzag GNRs (ZGNRs) are highly desirable for emerging applications in spintronics and quantum information technology as they can host spin-polarized states localized on their edges.^[20–22]

Nevertheless, the synthesis of ZGNRs and their structural diversification have remained a major challenge in the field, due to the geometric restriction imposed by precursor homo-coupling via single C–C bond formation, and consequently, only two similar design motifs have been reported to afford ZGNRs.^[23,24] In particular, the on-surface synthesis of the 6-atom-wide ZGNR (6-ZGNR), the first ZGNR synthesized with atomic precision, was based on 2,12-dibromo-14- R_1 -7- R_2 -benzo[*m*]tetraphene as the precursor, cleverly subverting the geometric restriction on polymerization (**Figure 1a**)^[23]: Upon debromination, polymerization occurred along the zigzag direction to form a snake-like polymer, leading to 6-ZGNR with a dimethylbiphenyl group as R_1 , through the surface-catalyzed oxidative cyclodehydrogena-

tion. The choice of various R_1 and R_2 substituents on the polymer backbone made available a platform for the conception of various GNRs with this motif. However, the synthesis of the corresponding precursor molecules is highly challenging due to the structural complexity and their thorough purification, which is essential for the on-surface polymerization, is not trivial because of their poor solubility. Consequently, only a few minor modifications of the precursor of 6-ZGNR have thus far been achieved,^[23,25,26] prohibiting the exploration of their structure dependent electronic properties, e.g., by incorporation of periodic edge-extension on to the zigzag edges.

Here, we introduce a design motif to synthesize ZGNRs with diverse periodic edge-extensions, a class of novel GNRs that we name edge-extended ZGNRs. This molecular motif relies on a simple 2,7-linked-9- R_1 -10- R_2 -anthracene polymer backbone achieved by the surface-catalyzed debromination and subsequent polymerization of 2,7-dibromo-9- R_1 -10- R_2 -anthracene (**Figure 1b**). The inter-molecular C–C bond is formed at an angle of 30° to the growth axis. This design motif entails the

incorporation of edge extensions fused onto the zigzag edge at alternating sides of the backbone, ruling out the synthesis of pristine ZGNRs. However, it provides a platform for synthesizing various types of edge-extended ZGNRs due to its versatility. Compared to benzo[*m*]tetraperenes, anthracenes are synthetically more accessible, as also seen in the large variety of surface-synthesized structures based on 10,10'-dibromo-9,9'-bianthracene, the precursor used to synthesize the prototypical 7-AGNR.^[12,15,27-29]

To establish the novel design motif based on 2,7-linked anthracenes, we synthesize a precursor with bianthryl substitution onto the R₁ position (Figure 1b). Annealing the molecular precursors on Au(111) single crystal surfaces under ultrahigh vacuum conditions yields an edge-extended 3-ZGNR with edge-fused bisanthene extensions, which we name the 3-ZGNR-E(bisanthene, 7) or 3-ZGNR-E(BA, 7) for brevity (see Section S1, Supporting Information for definition of the nomenclature). The chemical structure of the 3-ZGNR-E(BA, 7) is confirmed by bond-resolved non-contact atomic force microscopy (nc-AFM, Figure 1c). STM, STS, and Density functional theory (DFT) calculations provide further insights into its electronic properties.

2. Results and Discussion

The precursor 2,7-dibromo-9,9':10',9''-teranthracene (**6**) is designed to obtain the anthracene polymer backbone with a larger bianthryl (= R₁) substituent (Figure 2a). For the synthesis of **6**, 5-bromo-2-(4-bromobenzyl)benzaldehyde (**2**) was prepared by palladium-catalyzed C(sp³)-H arylation^[30] of 5-bromo-2-methylbenzaldehyde (**1**) with 1-bromo-4-iodobenzene (**2**) in 52% yield (Figure 2a). On the other hand, 10-bromo-9,9'-bianthracene (**5**) was obtained via bromination of 9,9'-bianthracene (**4**) with an equivalent amount of *N*-bromosuccinimide (NBS) in 40% yield. Bromide **5** was lithiated to (9,9'-bianthracen)-10-ylolithium, and subsequently reacted with aldehyde **2**, followed by cyclization with BF₃·OEt₂ and then oxidation with 2,3-dichloro-5,6-dicyano-1,4-benzoquinone (DDQ), providing precursor **6** in 52% yield (see Section S2, Supporting Information for details of synthesis and characterizations). As shown below, upon thermal activation on Au(111), **6** undergoes the envisaged sequence of surface-catalyzed reactions and yields a 3-ZGNR-E(BA, 7), i.e., a 3-ZGNR with edge-fused bisanthene extensions (Figure 2a).

Deposition of **6** onto a clean Au(111) surface results in large islands of self-assembled intact molecules (Figure 2b). Upon annealing to 170 °C, the molecules undergo debromination followed by homocoupling to yield polymers of **7** (Figure 2c). The STM image shows linear polymers arranged in self-assembled islands. The formation of linear polymers confirms that the bianthryl substituents do not sterically hinder access to the σ -radical formed by debromination in **6**, demonstrating the viability of the proposed 2,7-dibromo-9-R₁-10-R₂-anthracene design motif for edge-extended ZGNR synthesis. Annealing to 310 °C triggers cyclodehydrogenation, resulting in planar GNRs with fret-patterned edges characterizing the 3-ZGNR-E(BA, 7) (Figure 2d). The GNRs are found to grow reasonably long, with an average length of 9 nm (see Section S3, Supporting Information for the statistics) The atomically precise synthesis of 3-ZGNR-E(BA, 7) is confirmed with bond-resolved nc-AFM images on a 16-unit long

segment (Figure 1c). It clearly resolves the three zigzag rows constituting the 3-ZGNR backbone, the three additional short zigzag rows within the edge-fused bisanthene extensions and their terminating armchair edge segments.

The electronic state localized on the zigzag edge of graphene is topological in origin,^[31] and therefore it must be localized on the boundary of the system. In this picture, incorporating the bisanthene extensions onto the zigzag edge pushes that boundary locally further out. The edge state on the original zigzag “edge” of the “3-ZGNR” is thus locally quenched. Since the bisanthene extensions also possess zigzag edges, the edge state is now expected to be localized on this new boundary. These heuristic arguments are fully supported by spin-unrestricted DFT band structure calculations for the 3-ZGNR-E(BA, 7) in the gas phase (Figure 3a), that show the spin-polarized state hosted on the edges of this GNR (Figure 3b). DFT calculations neglecting spins (i.e., spin-restricted) reveal an ultralow bandgap of 0.01 eV. Incorporating the spin degree of freedom increases this bandgap to 0.24 eV. The states that are almost at the Fermi level in the spin-restricted case, the conduction band (CB) and the valence band (VB) at the Γ point, are both localized on the edges of the GNR (Figure 3c). When electron–electron interactions are included, it is more favorable for the electrons to spin-polarize, forming the so-called Mott–Hubbard gap. Indeed, based on the DFT calculations, the spin-polarized GNR is more stable by 35 meV and thus the open-shell electronic configuration better represents the ground state of the free standing system. Additionally, we perform tight-binding calculations with a mean-field Hubbard Hamiltonian to investigate the development of the magnetization as a function of the length and the strength of the on-site Coulomb repulsion (*U*). We find GNRs have spin polarized ege-states irrespective of their length at reasonable values of *U* (see Section S4, Supporting Information).

The characterization of ZGNRs with spin-polarized frontier states is challenging to achieve on metallic surfaces.^[23] Due to the spin polarization, the ZGNRs have an open-shell ground state, and consequently, these reactive GNRs can strongly couple to the metal surface. It required a decoupling layer of NaCl to unravel the intrinsic electronic properties of 6-ZGNR.^[23] Somewhat unexpectedly, the 3-ZGNR-E(BA, 7) exhibits spectroscopic signatures in scanning tunneling spectroscopy (STS) measurements even on the Au(111) surface (Figure 4a,b). The spectroscopic features are most pronounced near the ends of the GNR (see Section S5, Supporting Information for a discussion). Moreover, a constant-height current map at –10 mV bias reveals striking molecular orbital features, evidencing the presence of electronic states near the Fermi level, as opposed to a bandgap of ≈ 0.24 eV expected for the open-shell ground state of the GNR in gas-phase (Figure 3a).

The broad spectroscopic features deriving from these frontier states indicate significant hybridization with the underlying metal surface. To identify the origin of the observed spectral features, we acquired differential conductance (*dI/dV*) maps at various energies on a 9-unit long GNR (Figure 4e). These maps are in qualitative agreement with the gas-phase orbitals shown in Figure 3c, permitting us to assign these features to their origin in the spin-restricted band structure of the GNR. The corresponding points are indicated below the acquired images. On the Au(111) surface, the minimum of the second-highest valence

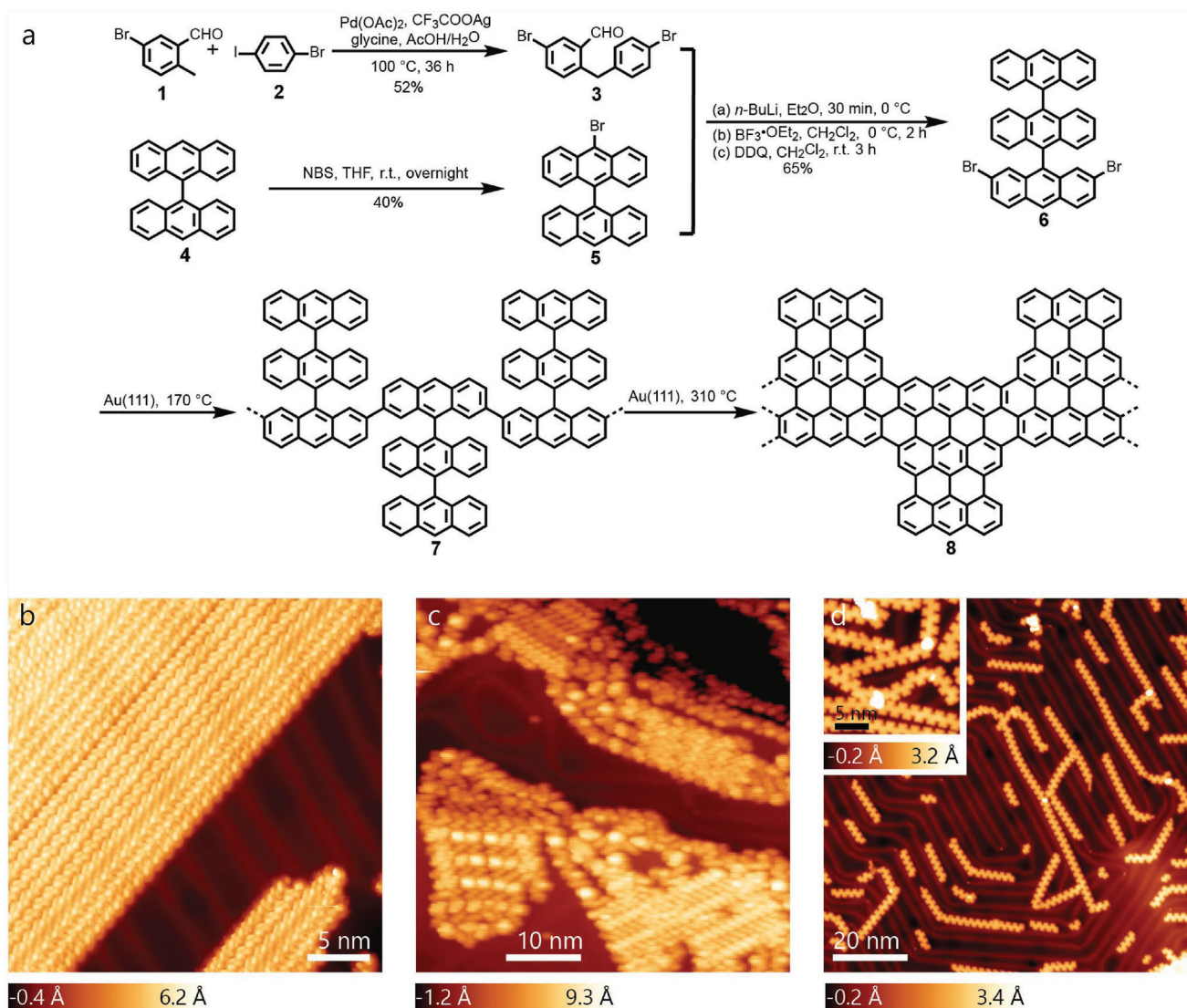


Figure 2. On-surface synthesis of 3-ZGNR-E(BA,7). a) Chemical schematic of the formation of 3-ZGNR-E(BA,7), **8**, on the Au(111) surface. b) STM image acquired after deposition of **6** on Au(111) with the molecules self-assembling into large islands ($V = -1$ V, $I = 50$ pA). c) STM image of the polymers formed after annealing to 170 °C ($V = -1$, $I = 20$ pA). d) Cyclodehydrogenation of the polymers is triggered above 300 °C, and long segments of 3-ZGNR-E(BA,7) are formed ($V = -1$ V, $I = 100$ pA). Inset: at higher coverages, the ends of the GNRs may fuse ($V = -1$ V, $I = 20$ pA). Color bars for (b)–(d) represent apparent height.

band (VB-1 Γ) is at -0.8 eV, and the maximum of the second conduction band (CB+1 Γ) is at 1.15 eV. This corresponds to a “bandwidth” of ≈ 2.0 eV for the four bands (CB+1, CB, VB, and VB-1), which is somewhat (and unsurprisingly) underestimated by the gas-phase DFT calculations (≈ 1.4 eV). The assignment above compared a finite GNR segment adsorbed onto a substrate with an infinite gas-phase GNR. The objective of such a comparison was to link the orbitals of a finite system to the bands of an infinite GNR. However, to capture the interaction of the GNRs with the metal substrate, we obtain the DFT-optimized geometry of a 9-unit segment of 3-ZGNR-E(BA,7) adsorbed on a 4-layer Au-slab. Spin-restricted STM (Figure 4c) and STS (Figure 4d) simulations were performed on the optimized geometry. The simulated STS results exhibit broad spectroscopic features. This shows that

the DFT calculations capture the hybridization between GNR and Au states, therefore provide a better comparison with the experimental observations than the gas phase calculations. Simulated dI/dV maps shown in Figure 4f are in qualitative agreement with the corresponding experimental results. A series of the simulated dI/dV maps from -1.0 to 1.0 eV in steps of 0.1 eV are shown in Section S6 (Supporting Information) and additional experimental results are shown in Section S7 (Supporting Information).

Experimentally, the broad spectroscopic features are largely confined to the ends of the GNR segment. Naively, one may be tempted to assign the peak near the Fermi level seen at the ends of the GNR (Figure 4b) to a “topological end-state.” However, this is clearly not the case. Tight-binding simulations of a finite length GNR segment exhibit no mid-gap end states, showing that the

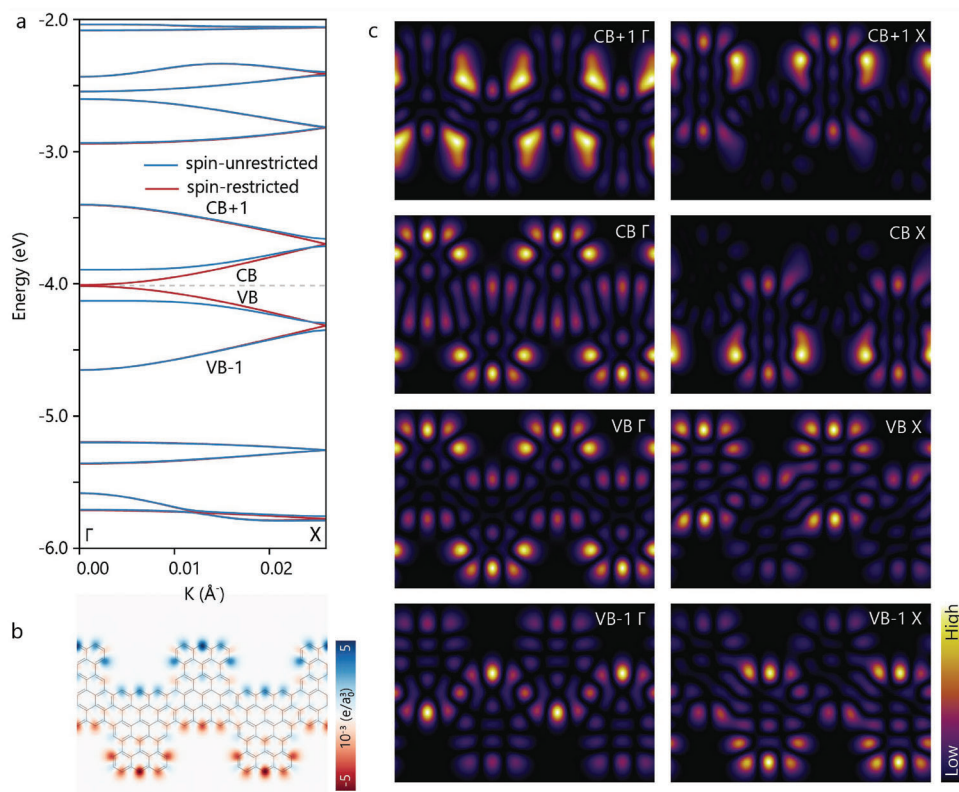


Figure 3. Gas phase band structure and frontier orbitals of the 3-ZGNR-E(BA, 7). a) Spin-restricted (in red) and spin-unrestricted (in blue) DFT band-structure calculations show a bandgap of 0.01 and 0.24 eV, respectively. The dashed grey line indicates the Fermi level for a charge neutral GNR, the first and second conduction and valence bands are labeled. The reciprocal space is shown from the Γ -point to the X-point. b) Spin density plot of the GNR. c) The spin-restricted gas phase orbitals of the GNR at the Γ - and X-points are shown for the first two conduction and valence bands. The images are labeled with the points in the band structure that they represent.

system is topologically trivial (see Section S8, Supporting Information). The origin of the high intensity of the STS signal at the ends of the GNR lies in the symmetry of the wavefunctions in the VB and CB, as has previously been observed for the armchair edges of the 7-AGNR.^[32,33] A detailed discussion of this effect is given in Section S5 (Supporting Information).

The absence of a substantial bandgap (>0.24 eV) shows that the GNR is closed-shell when adsorbed on Au(111), despite having an open-shell ground-state in gas-phase. To show that the interaction with the substrate leads to the loss of spin-polarization, we first obtain the gas phase orbitals of the adsorbed 9-unit GNR segment. We then calculate the projected density of states (PDOS) of all the states of the optimized GNR–Au substrate system onto these gas-phase orbitals. This is obtained by taking a dot product of the orbital wavefunctions with every state of the combined GNR–Au slab system. The corresponding plots (see Section S9, Supporting Information) reveal that the PDOS for each orbital is significantly broadened due to hybridization of the GNR with the Au-slab. Moreover, the gas phase HOMO, HOMO-1, and HOMO-2 of the 9-unit segment are substantially depopulated when the GNR is adsorbed onto the Au surface (Figure S10, Supporting Information). Similar depopulation has been observed in the case of the end-states of the 7-atom wide AGNR (7-AGNR).^[34] Depopulation of the states near VB Γ results in the 3-ZGNR-E(BA, 7) segment being closed-shell on Au(111).

However, the 7-AGNR end-states were re-populated when the 7-AGNR segments were transferred onto thin insulating NaCl decoupling layers.^[34,35] A similar strategy may enable us to uncover the open-shell ground state of 3-ZGNR-E(BA, 7).

Adsorption of 3-ZGNR-E(BA, 7) on the Au surface thus quenches its intrinsic magnetic properties, and electronic decoupling from the metal substrate is thus essential for exploring the expected intriguing magnetic properties.^[26] However, strong interaction of a GNR with the underlying metal surface makes the STM tip-assisted manipulation of a GNR segment on top of a NaCl layer highly challenging. The recent success in growing 7-AGNRs on a TiO₂ surface points to a possible alternative to electronically decouple GNRs,^[36] but is beyond the scope of the present work.

Recent results on a nitrogen-substituted 6-ZGNR suggest the possibility to spectroscopically access the edge states of the substituted 6-ZGNR even on the Au(111) surface, without the need for a decoupling layer.^[26] Similar nitrogen substitutions might also be achieved with the design motif presented here. Finally, we note that the work done here focused entirely on R₁ substituents. Future work could incorporate additional R₂ substituents on the polymer backbone to obtain wider ZGNRs, such as to decrease the hybridization between opposite zigzag edges. Successful incorporation of R₂ and R₁ substituents along with heteroatom substitutions provide a versatile route to the synthesis of various

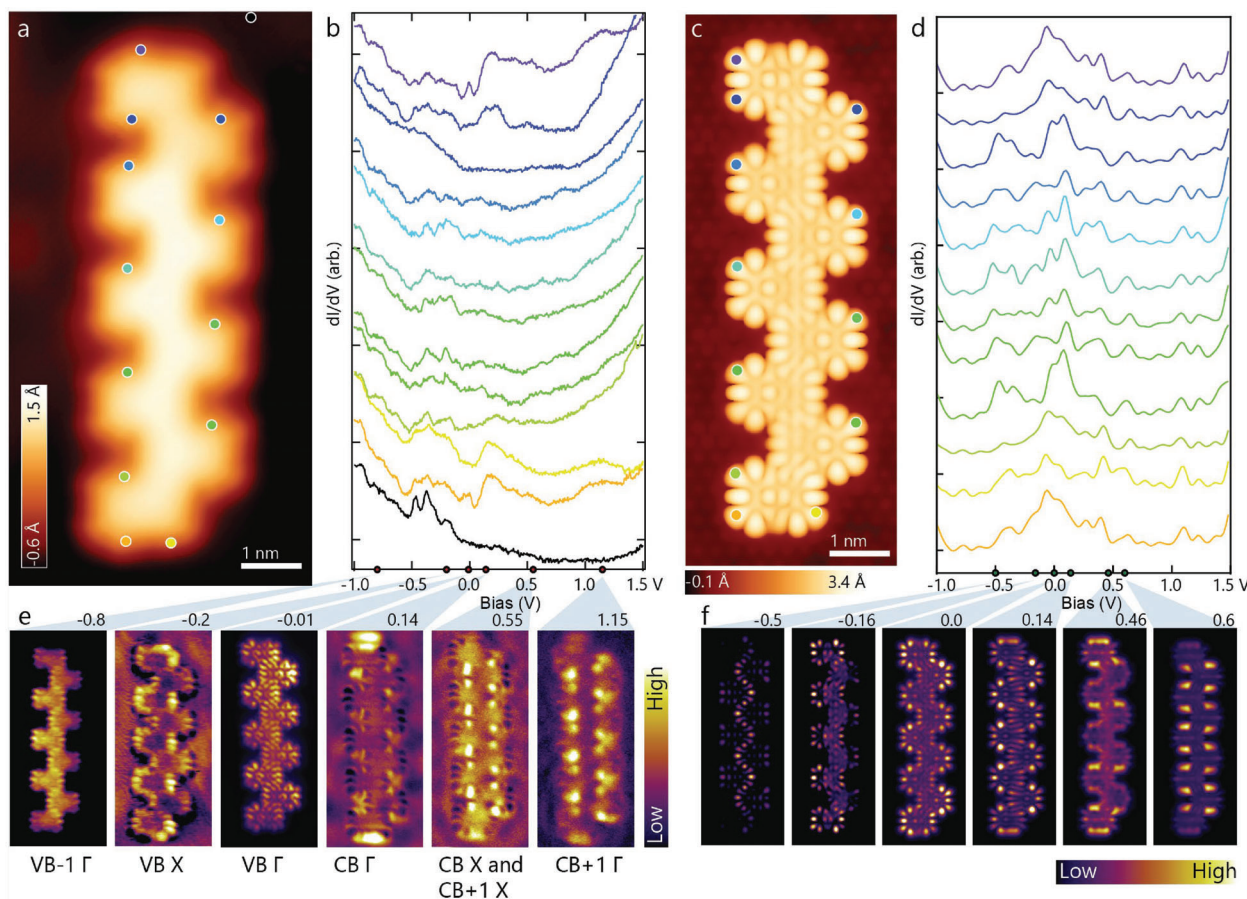


Figure 4. Electronic characterization of the 3-ZGNR-E(BA, 7) on Au(111). a,b) The STS measurements in (b) are acquired on the 9-unit GNR segment shown in (a), and the spectra are color-coded to their STS positions in (a). Broad spectroscopic features are seen around the Fermi level and near the ends of the GNR. c,d) STM and STS simulations on a DFT-optimized geometry of a 9-unit GNR segment on an Au(111) slab. The spectra shown in (d) are the local density of states (LDOS) as a function of energy, color-coded to their acquisition positions on the simulated STM image in (c). e) dI/dV maps acquired over the GNR shown in (a). Acquisition bias is shown above each map, and the best-fitting gas-phase orbital of an infinite GNR is indicated below each maps. f) Simulated dI/dV maps for the system shown in (c) that best fit the experimental results are shown with the corresponding energy indicated above the individual maps. (Tunneling parameters in (a): $V = -20$ mV, $I = 50$ pA. STS settings in (b): Feedback switched off over the indicated positions at -1 V, 250 pA. Simulation settings in (c): Simulated STM image with $V = -0.1$ V. d) simulated STS spectra by plotting the LDOS versus energy at 4 Å. Imaging conditions for the maps in (e): map at -0.8 V was acquired at a constant-height above the GNR, feedback loop switched off at -0.8 V, 200 pA on the GNR. The map at -0.01 V is the current-image acquired at a constant-height over the GNR, feedback loop switched off at -0.01 V, 100 pA. dI/dV maps at other biases are acquired with constant-current of 200 pA. dI/dV maps and STS in (b) were recorded with a peak-to-peak excitation voltage of 20 mV. (f): dI/dV maps are simulated at a constant-height of 4 Å above the GNR).

novel GNR structures utilizing this design motif. Their expected magnetic and optical properties make these systems technologically highly appealing.

3. Conclusion

We have developed a new bottom-up graphene nanoribbon design motif based on a family of 2,7-dibromo-9- R_1 -10- R_2 -anthracene precursors and deployed it for the successful on-surface synthesis of a novel edge-extended ZGNR. The essential characteristic of the 2,7-dibromo-9- R_1 -10- R_2 -anthracene design motif is its versatility, and several possible edge-extended ZGNRs can be attained with synthetically feasible modifications of the precursor. An intriguing possibility would be the incorporation of spinful edge-extensions that could interact via the

edge states. Moreover, the tremendous body of knowledge generated in synthesizing dibromo-bianthryl precursors for AGNRs is also applicable with the novel design motif to synthesize edge-extended ZGNRs. Heteroatom substitutions, incorporation of macrocycles, different edge morphologies, and GNR-heterojunctions, which were hitherto largely limited to AGNRs, are expected to now become available also in the zigzag direction.

4. Experimental Section

Sample Preparation: Details of the synthesis and characterizations of monomer **6** and all the other new compounds are reported in Section S2 (Supporting Information). Single crystal Au(111) substrates (MaTeck GmbH) were cleaned by repeated cycles of sputtering with Ar^+ ions

followed by annealing to 400–450 °C. Monomer **6** was deposited onto the cleaned Au(111) surface in situ by sublimating the precursor molecules from quartz crucibles. A custom built evaporator, by Lukas Rotach (Empa) was utilized to this end. A quartz crystal microbalance was used to ensure a sublimation rate corresponding to a rate of ≈ 2.3 monolayer h^{-1} . The on-surface synthesis was triggered by annealing the Au(111) single crystal at the specified temperature for 15–60 min. Longer times were used to trigger the polymerization, while shorter times were used to trigger cyclodehydrogenation. The surface temperature was measured with an optical pyrometer (Optris). The sample preparations were carried out in a preparation chamber (base-pressure: 2×10^{-10} mbar) and the samples then transferred to the attached STM chamber (base-pressure: 7×10^{-11} mbar).

The STM and nc-AFM experiments were performed using a low-temperature scanning tunneling microscope (Scienta Omicron) operated at 4.7 K with a tungsten tip placed on a qPlus tuning fork sensor.^[37] The tip was functionalized with a single CO molecule.^[38] The CO was deposited onto the surface by filling the STM chamber with the gas at a pressure of 3×10^{-8} mbar, with the sample in the cold STM stage. To pick up the CO molecule from the Au(111) surface, the surface at -20 mV and 120–200 pA was scanned till a change in height was observed. To perform the nc-AFM measurements, the qPlus sensor was driven at its resonance frequency (24787 Hz, quality factor 20.6k) with a constant amplitude < 100 pm. A phase-locked loop (PLL, HF2Li PLL by Zurich Instruments) was used to track the frequency shift of the tuning fork. The Δz values are measured with respect to the tip-surface distance where the feedback loop is switched off. Increasing Δz corresponds to increasing the tip-surface distance.

Computational Details: DFT computations were executed using the AiiDALab environment,^[39] based on AiiDA,^[40] and the CP2K code.^[41] Surface-adsorbate setups were modeled within a periodic slab scheme. The simulation cell included four Au atomic planes along the [111] orientation. Hydrogen atoms passivated one face of the slab to mitigate Au(111) surface states. A 40 Å vacuum layer was included to isolate the system from its periodic images along the axis orthogonal to the slab. Electronic wavefunctions were represented via TZV2P Gaussian basis set^[42] for C, H, and DZVP for Au. Plane-wave basis cutoff for the charge density was set at 600 Ry. Norm-conserving Goedecker–Teter–Hutter pseudopotentials^[43] were employed. The PBE GGA functional^[44] and included Grimme’s D3 scheme^[45] was adopted for van der Waals interactions. Au supercells varied in size depending on the adsorbate, ranging from $28.12 \times 26.54 \text{ \AA}^2$ (corresponding to 480 Au atoms) to $89.37 \times 32.42 \text{ \AA}^2$ (1728 Au atoms). Geometry optimization were performed with the bottom two atomic planes constrained while relaxing others until forces were below $0.005 \text{ eV \AA}^{-1}$. For nc-AFM studies in AiiDALab, equilibrium geometries and CP2K-calculated electrostatic potentials were used alongside Hapala’s probe-particle code.^[46]

STM simulations were based on the Tersoff–Hamann approximation,^[47] utilizing the Kohn–Sham orbitals of the slab and the adsorbate. Charge density decay was corrected by extrapolating orbitals to the vacuum. Band structure DFT for GNRs was carried out in Quantum Espresso,^[48] using PBE and a 400 Ry cutoff for charge density, along with PAW pseudopotentials and a $13 \times 1 \times 1$ k-grid. Convergence criteria for forces were set at 0.001 a.u. Molecular orbital projections were computed through scalar products with full-system orbitals, utilizing gas-phase molecular orbitals in their adsorption conformations.

The tight-binding (TB) calculations were performed by solving the standard MFH-Hamiltonian:

$$\hat{H}_{\text{TB}} = -t_1 \sum_{\langle i,j \rangle, \sigma} c_{i,\sigma}^\dagger c_{j,\sigma} - t_3 \sum_{\langle\langle i,k \rangle\rangle, \sigma} c_{i,\sigma}^\dagger c_{k,\sigma} + U \sum_{i,\sigma} \langle n_{i,\sigma} \rangle n_{i,\bar{\sigma}} - U \sum_i \langle n_{i,\uparrow} \rangle \langle n_{i,\downarrow} \rangle \quad (1)$$

where $c_{i,\sigma}^\dagger$ is the creation operator for an electron with spin σ at site i and $c_{j,\sigma}$ is the annihilation operator for an electron with spin σ at site j . σ can be either spin-up (\uparrow) or spin-down (\downarrow), with $\bar{\sigma}$ indicating the opposite spin component compared to σ . $\langle i, j \rangle$ are 1st nearest-neighbor pairs of the lat-

tice and $\langle\langle i, k \rangle\rangle$ are the 3rd nearest neighbor pairs. The hopping for nearest neighbor pairs, $t_1 = 3 \text{ eV}$ and the hopping over the 3rd nearest neighbor pairs, $t_3 = 0.3 \text{ eV}$, unless otherwise stated. Due to particle-hole symmetry the next nearest neighbor hopping (t_2) is set to zero. The on-site Coulomb repulsion term is also set to zero to simulate the non-magnetic system. To compute the magnetic properties of the gas-phase system, shown in Section S4 (Supporting Information), U is non-zero, where a typical value for U would be 3 eV, i.e., $1 \times t_1$. $n_{i,\sigma}$ denotes the spin-dependent number operator and $\langle n_{i,\sigma} \rangle$ is the mean occupation number at site i .

$|E_n\rangle$ are the eigenvectors of \hat{H}_{TB} : $|E_n\rangle = \sum_i \alpha_{i,n} |i\rangle$ with $|i\rangle$ as the vector-space basis of lattice sites. The wavefunctions in real-space are calculated using Slater $2p_z$ orbitals (ϕ_{2p_z}) at each site i .

$$\psi_n(\vec{r}) = \sum_i \alpha_{i,n} \phi_{2p_z}(\vec{r} - \vec{r}_i) \quad (2)$$

To simulate the dI/dV maps, LDOS(\vec{r}), shown in Section S5 (Supporting Information), the orbital electron densities were summed over the relevant energy window $[E_{n_1}, E_{n_2}]$:

$$\text{LDOS}(\vec{r}) = \sum_n |\psi_n(\vec{r})|^2, \quad n \in [n_1, n_2] \quad (3)$$

Supporting Information

Supporting Information is available from the Wiley Online Library or from the author.

Acknowledgements

A.K. and X.X. contributed equally to this work. This work was supported by the Swiss National Science Foundation (Grant No. 200020_212875), the NCCR MARVEL funded by the Swiss National Science Foundation (Grant No. 51NF40-182892), the Werner Siemens-Stiftung, the Okinawa Institute of Science and Technology Graduate University, and the Max Planck Society. Computational support from the Swiss Supercomputing Center (CSCS) under project ID s1141 is gratefully acknowledged. The authors acknowledge PRACE for awarding access to the Fenix Infrastructure resources at CSCS, which are partially funded from the European Union’s Horizon 2020 research and innovation program through the ICEI project under the grant agreement No. 800858. Technical support from Lukas Rotach is gratefully acknowledged.

Open access funding provided by ETH-Bereich Forschungsanstalten.

Conflict of Interest

The authors declare no conflict of interest.

Data Availability Statement

The data that support the findings of this study are available at the Materials Cloud Platform (DOI:10.24435/materialscloud:jx-k9).

Keywords

electronic properties, graphene nanoribbons, nc-AFM, on-surface synthesis, STM

Received: June 29, 2023
Revised: September 6, 2023
Published online: October 25, 2023

- [1] R. S. K. Houtsma, J. De La Rie, M. Stöhr, *Chem. Soc. Rev.* **2021**, 50, 6541.
- [2] S. Clair, D. G. De Oteyza, *Chem. Rev.* **2019**, 119, 4717.
- [3] L. Grill, S. Hecht, *Nat. Chem.* **2020**, 12, 115.
- [4] Q. Shen, H.-Y. Gao, H. Fuchs, *Nano Today* **2017**, 13, 77.
- [5] J. Cai, P. Ruffieux, R. Jaafar, M. Bieri, T. Braun, S. Blankenburg, M. Muoth, A. P. Seitsonen, M. Saleh, X. Feng, K. Müllen, R. Fasel, *Nature* **2010**, 466, 470.
- [6] L. Talirz, H. Söde, T. Dumslaff, S. Wang, J. R. Sanchez-Valencia, J. Liu, P. Shinde, C. A. Pignedoli, L. Liang, V. Meunier, N. C. Plumb, M. Shi, X. Feng, A. Narita, K. Müllen, R. Fasel, P. Ruffieux, *ACS Nano* **2017**, 11, 1380.
- [7] J. Yamaguchi, H. Hayashi, H. Jippo, A. Shiotari, M. Ohtomo, M. Sakakura, N. Hieda, N. Aratani, M. Ohfuchi, Y. Sugimoto, H. Yamada, S. Sato, *Commun. Mater.* **2020**, 1, 36.
- [8] A. Kimouche, M. M. Ervasti, R. Drost, S. Halonen, A. Harju, P. M. Joensuu, J. Sainio, P. Liljeroth, *Nat. Commun.* **2015**, 6, 10177.
- [9] Y.-C. Chen, D. G. De Oteyza, Z. Pedramrazi, C. Chen, F. R. Fischer, M. F. Crommie, *ACS Nano* **2013**, 7, 6123.
- [10] G. D. Nguyen, H.-Z. Tsai, A. A. Omrani, T. Marangoni, M. Wu, D. J. Rizzo, G. F. Rodgers, R. R. Cloke, R. A. Durr, Y. Sakai, F. Liou, A. S. Aikawa, J. R. Chelikowsky, S. G. Louie, F. R. Fischer, M. F. Crommie, *Nat. Nanotechnol.* **2017**, 12, 1077.
- [11] J. D. Teeter, P. Zahl, M. Mehdi Pour, P. S. Costa, A. Enders, A. Sinitskii, *ChemPhysChem* **2019**, 20, 2281.
- [12] C. Moreno, M. Vilas-Varela, B. Kretz, A. Garcia-Lekue, M. V. Costache, M. Paradinas, M. Paniguel, G. Ceballos, S. O. Valenzuela, D. Peña, A. Mugarza, *Science* **2018**, 360, 199.
- [13] Q. Sun, O. Gröning, J. Overbeck, O. Braun, M. L. Perrin, G. Borin Barin, M. El Abbassi, K. Eimre, E. Ditler, C. Daniels, V. Meunier, C. A. Pignedoli, M. Calame, R. Fasel, P. Ruffieux, *Adv. Mater.* **2020**, 32, 1906054.
- [14] D. J. Rizzo, G. Veber, T. Cao, C. Bronner, T. Chen, F. Zhao, H. Rodriguez, S. G. Louie, M. F. Crommie, F. R. Fischer, *Nature* **2018**, 560, 204.
- [15] O. Gröning, S. Wang, X. Yao, C. A. Pignedoli, G. Borin Barin, C. Daniels, A. Cupo, V. Meunier, X. Feng, A. Narita, K. Müllen, P. Ruffieux, R. Fasel, *Nature* **2018**, 560, 209.
- [16] J. Yin, P. H. Jacobse, D. Pyle, Z. Wang, M. F. Crommie, G. Dong, *J. Am. Chem. Soc.* **2022**, 144, 16012.
- [17] P. Han, K. Akagi, F. Federici Canova, H. Mutoh, S. Shiraki, K. Iwaya, P. S. Weiss, N. Asao, T. Hitosugi, *ACS Nano* **2014**, 8, 9181.
- [18] A. Keerthi, C. Sánchez-Sánchez, O. Deniz, P. Ruffieux, D. Schollmeyer, X. Feng, A. Narita, R. Fasel, K. Müllen, *Chem. Asian J.* **2020**, 15, 3807.
- [19] J. Li, S. Sanz, N. Merino-Díez, M. Vilas-Varela, A. Garcia-Lekue, M. Corso, D. G. De Oteyza, T. Frederiksen, D. Peña, J. I. Pascual, *Nat. Commun.* **2021**, 12, 5538.
- [20] K. Nakada, M. Fujita, G. Dresselhaus, M. S. Dresselhaus, *Phys. Rev. B* **1996**, 54, 17954.
- [21] K. Wakabayashi, K.-I. Sasaki, T. Nakanishi, T. Enoki, *Sci. Technol. Adv. Mater.* **2010**, 11, 054504.
- [22] M. Fujita, K. Wakabayashi, K. Nakada, K. Kusakabe, *J. Phys. Soc. Jpn.* **1996**, 65, 1920.
- [23] P. Ruffieux, S. Wang, B. Yang, C. Sánchez-Sánchez, J. Liu, T. Dienel, L. Talirz, P. Shinde, C. A. Pignedoli, D. Passerone, T. Dumslaff, X. Feng, K. Müllen, R. Fasel, *Nature* **2016**, 531, 489.
- [24] Y. Fu, H. Yang, Y. Gao, L. Huang, R. Berger, J. Liu, H. Lu, Z. Cheng, S. Du, H.-J. Gao, X. Feng, *Angew. Chem.* **2020**, 132, 8958.
- [25] P. P. Shinde, J. Liu, T. Dienel, O. Gröning, T. Dumslaff, M. Mühlhous, A. Narita, K. Müllen, C. A. Pignedoli, R. Fasel, P. Ruffieux, D. Passerone, *Carbon* **2021**, 175, 50.
- [26] R. E. Blackwell, F. Zhao, E. Brooks, J. Zhu, I. Piskun, S. Wang, A. Delgado, Y.-L. Lee, S. G. Louie, F. R. Fischer, *Nature* **2021**, 600, 647.
- [27] R. R. Cloke, T. Marangoni, G. D. Nguyen, T. Joshi, D. J. Rizzo, C. Bronner, T. Cao, S. G. Louie, M. F. Crommie, F. R. Fischer, *J. Am. Chem. Soc.* **2015**, 137, 8872.
- [28] G. D. Nguyen, F. M. Toma, T. Cao, Z. Pedramrazi, C. Chen, D. J. Rizzo, T. Joshi, C. Bronner, Y.-C. Chen, M. Favaro, S. G. Louie, F. R. Fischer, M. F. Crommie, *J. Phys. Chem. C* **2016**, 120, 2684.
- [29] S. Kawai, S. Nakatsuka, T. Hatakeyama, R. Pawlak, T. Meier, J. Tracey, E. Meyer, A. S. Foster, *Sci. Adv.* **2018**, 4, 7181.
- [30] F.-L. Zhang, K. Hong, T.-J. Li, H. Park, J.-Q. Yu, *Science* **2016**, 351, 252.
- [31] W. Yao, S. A. Yang, Q. Niu, *Phys. Rev. Lett.* **2009**, 102, 096801.
- [32] H. Söde, L. Talirz, O. Gröning, C. A. Pignedoli, R. Berger, X. Feng, K. Müllen, R. Fasel, P. Ruffieux, *Phys. Rev. B* **2015**, 91, 045429.
- [33] S. E. Ammerman, V. Jelic, Y. Wei, V. N. Breslin, M. Hassan, N. Everett, S. Lee, Q. Sun, C. A. Pignedoli, P. Ruffieux, R. Fasel, T. L. Cocker, *Nat. Commun.* **2021**, 12, 6794.
- [34] S. Wang, L. Talirz, C. A. Pignedoli, X. Feng, K. Müllen, R. Fasel, P. Ruffieux, *Nat. Commun.* **2016**, 7, 11507.
- [35] N. Friedrich, P. Brandimarte, J. Li, S. Saito, S. Yamaguchi, I. Pozo, D. Peña, T. Frederiksen, A. Garcia-Lekue, D. Sánchez-Portal, J. I. Pascual, *Phys. Rev. Lett.* **2020**, 125, 146801.
- [36] M. Kolmer, A.-K. Steiner, I. Izydorczyk, W. Ko, M. Engelund, M. Szymanski, A.-P. Li, K. Amsharov, *Science* **2020**, 369, 571.
- [37] F. J. Giessibl, *Appl. Phys. Lett.* **2000**, 76, 1470.
- [38] L. Bartels, G. Meyer, K.-H. Rieder, D. Velic, E. Knoesel, A. Hotzel, M. Wolf, G. Ertl, *Phys. Rev. Lett.* **1998**, 80, 2004.
- [39] A. V. Yakutovich, K. Eimre, O. Schütt, L. Talirz, C. S. Adorf, C. W. Andersen, E. Ditler, D. Du, D. Passerone, B. Smit, N. Marzari, G. Pizzi, C. A. Pignedoli, *Comput. Mater. Sci.* **2021**, 188, 110165.
- [40] G. Pizzi, A. Cepellotti, R. Sabatini, N. Marzari, B. Kozinsky, *Comput. Mater. Sci.* **2016**, 111, 218.
- [41] J. Hutter, M. Iannuzzi, F. Schiffrmann, J. VandeVondele, *Wiley Interdiscip. Rev.: Comput. Mol. Sci.* **2014**, 4, 15.
- [42] J. Vandevondele, J. Hutter, *J. Chem. Phys.* **2007**, 127, 114105.
- [43] S. Goedecker, M. Teter, J. Hutter, *Phys. Rev. B* **1996**, 54, 1703.
- [44] J. P. Perdew, K. Burke, M. Ernzerhof, *Phys. Rev. Lett.* **1996**, 77, 3865.
- [45] S. Grimme, J. Antony, S. Ehrlich, H. Krieg, *J. Chem. Phys.* **2010**, 132, 154104.
- [46] P. Hapala, G. Kichin, C. Wagner, F. S. Tautz, R. Temirov, P. Jelínek, *Phys. Rev. B* **2014**, 90, 085421.
- [47] J. Tersoff, D. R. Hamann, *Phys. Rev. B* **1985**, 31, 805.
- [48] P. Giannozzi, O. Barone, P. Bonfà, D. Brunato, R. Car, I. Carnimeo, C. Cavazzoni, S. De Gironcoli, P. Delugas, F. Ferrari Ruffino, A. Ferretti, N. Marzari, I. Timrov, A. Urru, S. Baroni, *J. Chem. Phys.* **2020**, 152, 154105.